Discrete Material and Thickness Optimization of sandwich structures

Sjølund, J. H.; Peeters, D.; Lund, E.

Published in:
Composite Structures

DOI (link to publication from Publisher):
10.1016/j.compstruct.2019.03.003

Publication date:
2019

Document Version
Accepted author manuscript, peer reviewed version

Paper C

Discrete Material and Thickness Optimization of sandwich structures

J. H. Sjølund, D. Peeters, E. Lund

The paper has been submitted to Composite Structures

The layout has been revised.

Abstract

In this paper Discrete Material and Thickness Optimization (DMTO) is used to optimize sandwich composite structures subject to both displacement and linear buckling constraints. Using a new thickness formulation where density design variables scale ply thicknesses rather than constitutive properties, it is possible to size both core and face sheet plies simultaneously. This makes it possible to have different ply thicknesses for core and face sheet layers while also covering ply-drops. Furthermore, separating core and face sheets allows enforcing a symmetric lay-up which can be important to avoid warping during curing. The approach is demonstrated in three numerical examples of increasing complexity.

Keywords Discrete material and thickness optimization; laminated composites; sandwich structures

C.1 Introduction

Sandwich panels play an important role in many laminated composite structures. A modern wind turbine blade is an example of a laminated composite structure, and in this work the use of sandwich panels will mainly be discussed in this context. In wind turbine blades sandwich panels are used to carry shear loads in a weight-efficient manner while preventing local buckling. The internal shear webs carry the shear load resulting from flapwise loads, and the sandwich parts in the aerodynamic shell carry the shear load from edgewise loads. A typical wind turbine blade cross section with flapwise and edgewise load directions can be seen in Figure C.1. The use of sandwich panels in wind turbine blades is described in more detail in Thomsen (2009).

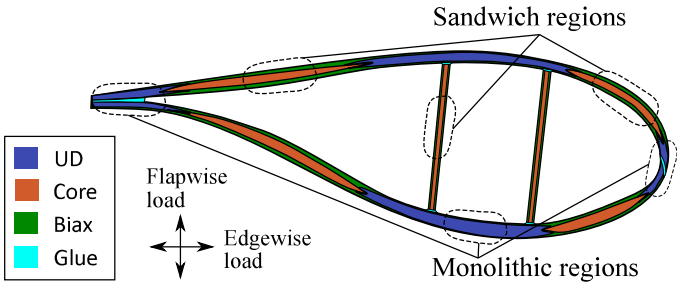

Fig. C.1: Typical wind turbine blade cross section. Monolithic regions are mainly uni-directional (UD) plies, while sandwich regions often use biaxial angle plies ($\pm 45°$) as face sheets, and balsa or foam as core material.

Sandwich panels in wind turbine blades often use PVC foam or balsa wood as the core material. Balsa is available as flexible grid-scored panels and a sample can be seen in Figure C.2. Flexible panels conveniently allow placing material in double curved molds. Furthermore, the cuts allow resin flow during the infusion process. Balsa panels are available in various thicknesses, typically ranging from 1/4 inch (6.35 mm), up to approximately 50 mm. On each side the sandwich core is covered by face sheets, sometimes called skins. The sandwich face sheets used in wind turbine

blades typically consist of several glass fiber reinforced plastic (GFRP) plies. Often GFRP biaxial angle plies of $\pm 45^\circ$ are used to provide damage tolerance and high shear stiffness.

Fig. C.2: Flexible end-grain balsa panel (Courtesy of nord compensati).

Many composite structures are variable stiffness structures with both varying thickness and varying lay-up. When it comes to determining the lay-up throughout the structure, structural optimization is often essential. Recent reviews on optimization of laminated composite structures can be seen in Nikbakt et al. (2018) and Xu et al. (2018). From these reviews it is clear that heuristic methods, such as genetic algorithms, are very popular for optimization of laminated composite structures. Heuristic methods are convenient since they can handle discrete design variables without modification. Discrete design variables can represent an integer number of plies or the choice of fiber angle from a finite set of candidates, such as $\pm 45^\circ, 0^\circ$, and 90°. Recent examples of the application of genetic algorithms to determine the lay-up of wind turbine blades can be found in Pirrera et al. (2012), Chen et al. (2013), Barnes and Morozov (2016), and in Albanesi et al. (2018).

The more general case of optimizing composite panels using heuristic methods while considering manufacturability is studied in, e.g., Kim et al. (1999), Kristinsdottir et al. (2001), Soremekun et al. (2002), Adams et al. (2004), Irisarri et al. (2014), and Fan et al. (2016). Kim et al. (1999) divide a structure into patches, which are then individually optimized with regard to the patchwise number of plies and fiber angles. Kristinsdottir et al. (2001) ensure continuity of plies across different panels (blending) by defining a key panel from which each ply emanates to adjacent regions. Adams et al. (2004), instead use a guide-based blending. Here the lay-up of all panels can be obtained by removing a number of plies from the guide laminate. Irisarri et al. (2014) use guide-based blending combined with a large number of manufacturing constraints to optimize a 18-panel test problem. However, in general, while heuristic methods are convenient for composite structures, they become computationally demanding for many design variables.

For a larger number of design variables gradient-based methods are more efficient, but require the design variables to be continuous. Examples of the sizing of wind turbine blades using gradient-based methods while considering the lay-up in terms of continuous thicknesses can be found in Bottasso et al. (2014), Forcier and Joncas (2012), Buckney et al. (2013), and Sjølund and Lund (2018). However, the use of continuous variables comes with the disadvantage that subsequent post-processing is

required to obtain a manufacturable lay-up (for example rounding thicknesses to a finite number of plies).

Another approach which can improve manufacturability is multi-step methods where successive optimizations are performed iteratively. Examples of multi-step methods can be found in, e.g., IJsselmuiden et al. (2009); Bloomfield et al. (2009); Liu et al. (2011); Irisarri et al. (2016); Peeters and Abdalla (2016). IJsselmuiden et al. (2009) first take thicknesses and lamination parameters as continuous design variables, and then secondly use a discrete guide laminate approach to ensure blending. Bloomfield et al. (2009) and Liu et al. (2011) use a similar approach, while the latter also compare results to a smeared stiffness approach. Irisarri et al. (2016) and Peeters and Abdalla (2016), a combination of subsequent thickness, fiber angle, and stacking sequence optimizations are performed to retrieve high performance fiber steered and variable thickness panels.

A gradient-based method which allows each ply to choose between a number of candidate materials is the Discrete Material Optimization (DMO) method in Stegmann and Lund (2005). The candidate materials can simply correspond to different fiber angles, but can also include, e.g., a core material candidate. To avoid (or limit) the amount of post-processing, intermediate values of design variables are penalized in order to obtain an (almost) discrete result. This method is used to optimize a wind turbine main spar subject to multiple criteria in Lund et al. (2008). An extension to the DMO method is the shape function with penalization (SFP) parameterization by Bruyneel (2011), which can reduce the number of candidate design variables. This is done by letting each of the four vertices in a 2D natural coordinate system represent a candidate, and using shape functions to calculate candidate weights. This approach is extended to 3 and 8 candidate materials in Bruyneel et al. (2011), and generalized to any number of candidates with the bi-valued coding with penalization (BCP) approach by Gao et al. (2012).

A development of this method is Discrete Material and Thickness Optimization (DMTO) which, in addition to material candidate choices, allow for thickness changes, see Sørensen and Lund (2013); Sørensen et al. (2014) and Gao et al. (2013). In this method each ply also has a density design variable (ranging from 0-1) that determines if there should be material or not, like in topology optimization. The choice of material or not in a certain layer is in practice accomplished by scaling constitutive properties. The DMTO method has recently been extended by a new thickness formulation in Sjølund et al. (2018). With the new thickness formulation, the density variables scale ply thicknesses rather than the constitutive properties. The new thickness formulation thereby allows for internal ply-drops without causing non-physical voids.

This paper will show how the DMTO method combined with the new thickness formulation can be used to simultaneously find the optimal number of core and face sheet layers in a sandwich structure, while also considering multiple fiber angle choices for each of the face sheet plies. Furthermore, it will be shown how the new thickness formulation also allows enforcing a symmetric lay-up, which is important to avoid warping during curing. Moreover, it allows ply-drops to be covered which is essential to avoid delaminations. Finally, the approach will be demonstrated in a number of numerical examples with multiple conflicting structural criteria such as buckling and displacement.

The DMTO method including manufacturing constraints is described in Section C.2. The used optimization approach is explained in Section C.3. The method and optimization approach are demonstrated in three numerical examples in Section C.4. Finally, the conclusion is given in Section C.5.

C.2 Method

C.2.1 Parameterization

In the DMTO method there are both density and material candidate design variables. A density design variable determines if there should be material or not in a layer within a given domain. The density design variable vector $\boldsymbol{\rho}$ is defined such that:

$$\rho_{dl} = \begin{cases} 1 \text{ if there is material in layer } l \text{ of domain } d \\ 0 \text{ otherwise} \end{cases} \tag{C.1}$$

Furthermore, material candidate design variables allow each layer within a patch to choose between different material candidates. Candidate materials can either be different fiber angles (e.g. UD/0°, UD/90° etc.), entirely different materials (UD/0°, Balsa), or a combination. The material candidate design variable vector $\mathbf{x}$ is defined such that:

$$x_{plc} = \begin{cases} 1 \text{ if candidate } c \text{ is selected in layer } l \text{ of patch } p \\ 0 \text{ otherwise} \end{cases} \tag{C.2}$$

Here both patches and domains refer to groups of finite elements. The distinction between patches and domains allows individual parameterizations for both densities and material candidates. An example of this is shown in Figure C.3. In this figure every element is also a domain, while there is only one patch containing all elements. Consequently, in a given layer the candidate choice is the same for all elements, while the density can vary in each layer in every element.

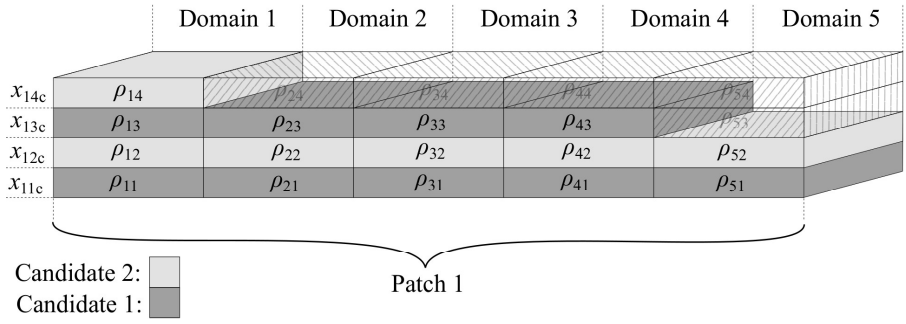

Fig. C.3: Example of parameterization into domains and patches. Here each element is a domain, while all elements are included in the single material candidate patch. Hatched layers represent zero density.

The usual method to include material candidate design variables in the problem, is to relax the integer requirement of the design variables and let the constitutive properties be a weighted sum of each of the candidate constitutive properties. If $\mathbf{E}_c$ is

the constitutive properties of candidate c, then the effective constitutive properties of layer l in element e can be written as:

$$\mathbf{E}_{el} = \sum_{c=1}^{n_c} x_{plc} \mathbf{E}_c, \quad x_{plc} \in [0;1] \tag{C.3}$$

where n_c is the number of candidate materials. To ensure a material choice it is required that the sum of material candidates is equal to one, i.e.:

$$\sum_{c=1}^{n_c} x_{plc} = 1, \quad \forall (p,l) \tag{C.4}$$

To favor discrete design variables implicit penalization is used. Implicit penalization is used to reduce constitutive properties for intermediate design variables. For multiple candidate materials penalization schemes can be found in, e.g., Hvejsel and Lund (2011). The multiphase RAMP (rational approximation of material properties) scheme, originally introduced in Stolpe and Svanberg (2001), is given as:

$$w(\mathbf{x}) = \frac{x_{plc}}{1 + p\left(1 - x_{plc}\right)} \tag{C.5}$$

where p is a penalization factor. To introduce penalization in the formulation (C.3) is re-written to:

$$\mathbf{E}_{el} = \sum_{c=1}^{n_c} w(\mathbf{x}) \mathbf{E}_c, \quad x_{plc} \in [0;1] \tag{C.6}$$

The RAMP scheme is shown in Figure C.4 where it can be seen that a design variable $x_{plc} = 0.5$ only provides 17% stiffness for 50% mass when using a penalization factor of $p = 4$.

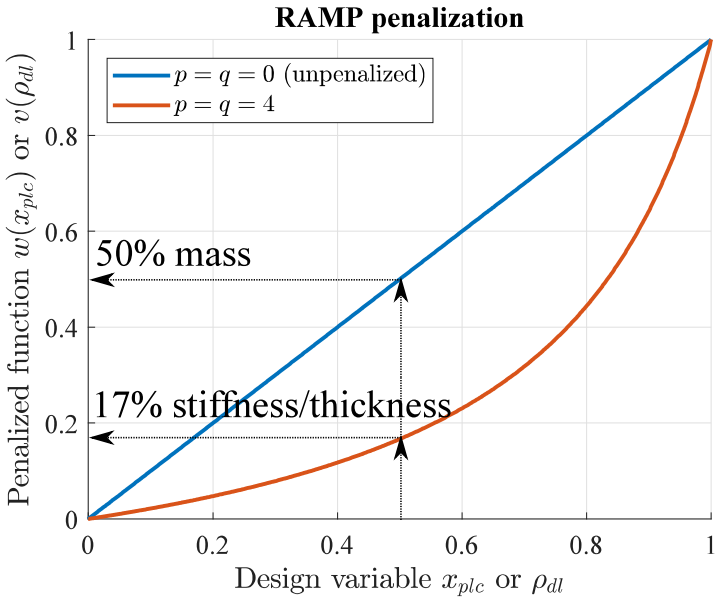

Fig. C.4: The RAMP penalization scheme for $p = q = 0$ (no penalization) and $p = q = 4$.

The density design variables are used to scale the ply thicknesses. The approach of scaling ply thicknesses rather than constitutive properties is introduced in the recent work by Sjølund et al. (2018). With this approach a density of one corresponds to the real ply thickness, a density of zero results in zero ply thickness, and intermediate densities yield intermediate pseudo ply thicknesses. This corresponds to a thickness in layer l element e of:

$$\tilde{t}_{el} = \rho_{dl} t_{pl} \tag{C.7}$$

where t_{pl} is the physical ply thickness of the material candidates of layer l in patch p, assuming that these candidates have the same physical ply thickness. Again, to favor discrete density design variables, a RAMP scheme is used such that:

$$v(\boldsymbol{\rho}) = \frac{\rho_{dl}}{1 + q(1 - \rho_{dl})} \tag{C.8}$$

where q is a penalization factor. Substituting (C.8) into (C.7), the effective ply thickness is written as:

$$\tilde{t}_{el} = v(\boldsymbol{\rho}) t_{pl} \tag{C.9}$$

Again the RAMP scheme is shown in Figure C.4 where it can be seen that a density of $\rho_{dl} = 0.5$ corresponds to a ply thickness of 17% of the physical ply thickness for 50% mass when using a penalization factor of $q = 4$. The multiphase SIMP scheme in Hvejsel and Lund (2011) has also been implemented for both density and material candidate design variables, but for simplicity only results obtained using the RAMP scheme are presented. Numerical tests have shown very similar performance of the two schemes for the examples presented.

Introducing the density design variables completes the parameterization, which can be summarized as:

$$\mathbf{E}_{el} = \sum_{c=1}^{n_c} w(\mathbf{x}) \mathbf{E}_c \tag{C.10}$$

$$\tilde{t}_{el} = v(\boldsymbol{\rho}) t_{pl} \tag{C.11}$$

$$\sum_{c=1}^{n_c} x_{plc} = 1 \quad \forall (\rho, l) \tag{C.12}$$

$$\rho_{el} \in [0;1] \quad \forall (e, l) \tag{C.13}$$

$$x_{plc} \in [0;1] \quad \forall (p, l, c) \tag{C.14}$$

In this paper the parameterization is demonstrated in three examples where the structural mass is minimized while subject to a combination of either compliance, displacement, or buckling constraints. In these cases zero thickness plies are unproblematic. However, allowing for zero thickness plies in laminate design with strength constraints may result in singular optima as demonstrated in Bruyneel and Duysinx (2006). For the standard DMTO approach it has been demonstrated in Lund (2018) how strength constraints can be included by using suitable penalization factors that are different from those that interpolate stiffness parameters, in order to remove the singular optima problem. However, for the new thickness formulation demonstrated in this paper the inclusion of strength constraints is left for future work.

C.2.2 Comparison with the original DMTO

In the original DMTO method, see Sørensen and Lund (2013), Sørensen et al. (2014), and Sørensen and Lund (2015), density design variables scale constitutive properties rather than ply thicknesses (like the candidate design variables). A consequence of the original approach is that intermediate voids arise if material is not removed from the top, as visualized in Figure C.5 (left). With the new thickness formulation, where densities scale ply thicknesses, intermediate voids can no longer occur, see Figure C.5 (right).

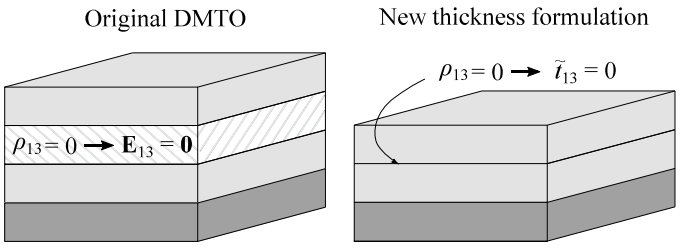

Fig. C.5: Visualization of a density change in the original DMTO method (left) and with the new thickness formulation (right). In the original DMTO method density variables scale the constitutive properties, and thereby intermediate voids can occur. In the new thickness formulation density variables scale ply thicknesses instead.

C.2.3 DMTO for sandwich structures

The new thickness formulation adds new possibilities regarding utilization of DMTO for manufacturable sandwich structures. First it is possible to size both inner core layers and outer face sheet layers simultaneously without introducing intermediate voids. The separation of core and face sheet plies makes it possible to have individual constraints on, e.g., the number of face sheet and core plies respectively. This separation also makes it possible to have different ply thicknesses for core and face sheet layers which is very relevant when using balsa as core material in combination with GFRP for face sheet layers. Next, since material does not have to be removed from the top, it is straightforward to constrain the face sheets to be symmetric around the core. Enforcement of symmetry removes the membrane-bending coupling which may be important to avoid warping during curing. Furthermore, the number of design variables can potentially be halved. Moreover, the new thickness formulation also makes it possible to cover ply-drops with continuous external plies which is important to avoid delaminations. Hence the parameterization allows determining both the discrete number of face sheet plies, face sheet fiber angles, the total core thickness as a multiple of a base plate thickness (e.g. 1/4"), while simultaneously ensuring a symmetric and manufacturable result.

The approach of separating core and face sheet layers is exemplified in Figure C.6. Here the dashed lines divide the eight layers through-the-thickness into a number of groups. The first group is the two outer layers 1 and 8 shown in green. These outer layers should always be present in order to cover ply-drops and also ensure at least one face sheet layer. The next group is a number of additional face sheet plies,

layers 2-3 and 6-7 shown in grey, which may be required for sufficient stiffness and strength. Moreover, in all face sheet layers, a number of candidate materials (fiber angles) are present. Finally, the last group is the core layers, shown in orange. Here the core layers are shown as balsa which has a different ply thickness than the face sheet layers.

In this example it can also be seen that the ply-dropping order is fixed in advance. For the additional face sheet plies, those closest to the outer surface are removed first such that $\rho_{13} > \rho_{12}$, and $\rho_{16} > \rho_{17}$, while core plies are simply removed from the top. The method used to enforce the ply-dropping order is slightly more complicated than simply constraining, e.g., $\rho_{16} > \rho_{17}$. Instead, so-called thickness constraints are used, explained in more detail in Section C.2.4.

The parameterization shown in Figure C.6 can be thought of as a guide laminate for all elements grouped in a material candidate patch. The lay-up of all domains located in the patch can be formed from the guide laminate. Taking offset in Figure C.3, but using the guide laminate in Figure C.6, an example of a feasible and locally symmetric lay-up is shown in Figure C.7. Also shown in this figure is the thickness of dummy layers. Dummy layers have close to zero stiffness and can be used in combination with mid-plane reference shell elements to obtain an offset material removal during optimization. The dummy layer approach is explained in more detail in Sjølund et al. (2018).

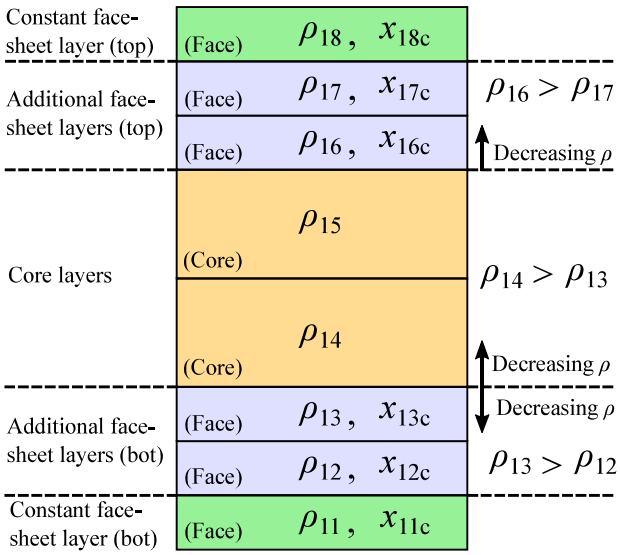

Fig. C.6: Parameterization allowing the simultaneous sizing of groups of face sheet and core layers.

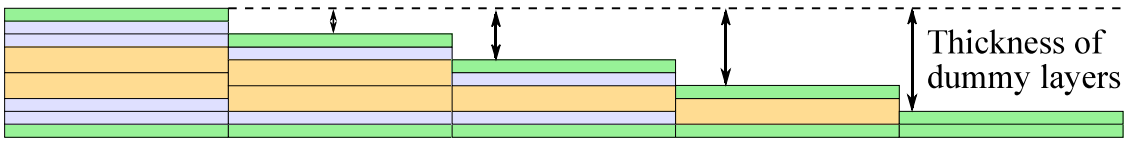

Fig. C.7: An example of a feasible variable thickness lay-up of five elements based on the parameterization shown in Figure C.6.

C.2.4 Manufacturing constraints

Thickness constraints (Ply-drop order)

In the original DMTO method, Sørensen and Lund (2013) formulated thickness constraints to prevent 'density bands'. Density bands correspond to densities through-the-thickness settling on the same intermediate value. These thickness constraints prevent density bands by enforcing a difference in density in subsequent layers. Thickness constraints work by limiting the maximum density in layer $l+1$ based on the current density in layer l such that:

$$\rho_{d(l+1)} \leq f\left(\rho_{dl}, T\right) \tag{C.15}$$

where f is a piecewise linear function defined as:

$$f\left(\rho_{dl}, T\right) = \begin{cases} f_1\left(\rho_{dl}, T\right) = a_1 \rho_{dl}, & \text{if } \rho_{dl} \leq 1 - T \\ f_2\left(\rho_{dl}, T\right) = a_2 \rho_{dl} + b_2, & \text{otherwise} \end{cases} \tag{C.16}$$
$$\text{where} \quad a_1 = \frac{T}{1-T}, \quad a_2 = \frac{1}{a_1}, \quad b_2 = \frac{2T-1}{T}$$

and T is a parameter in the range $0 < T \leq 0.5$ that controls the slope of f_1 and f_2. For $T = 0.5$ the equation reduces to $\rho_{d(l+1)} \leq \rho_{dl}$. The thickness constraint is plotted for different values of the T parameter in Figure C.8. The influence of the T parameter on the maximum allowable density in subsequent layers is visualized in Figure C.9.

Thickness constraints also govern the ply-drop order. In the original DMTO method, plies are always removed from the top to prevent intermediate voids. However, intermediate voids can not occur with the new thickness formulation, and hence any ply-drop order can be used.

In this paper thickness constraints are defined individually for core plies, additional face sheet layers above the core (top), and additional face sheet layers below the core (bot), in the directions shown with arrows in Figure C.6. In this figure, the thickness constraint for the core plies corresponds to $\rho_{d5} \leq f\left(\rho_{d4}, T\right)$. Denoting c_1 as the first core layer and c_e as the last core layer, the core thickness constraints can generally be written as:

$$\rho_{d(l+1)} \leq f\left(\rho_{dl}, T\right), \quad \forall d, \quad l = c_1, c_1+1, \ldots, c_e - 1 \tag{C.17}$$

For the additional face sheet layers above the core (top), this can similarly be written as:

$$\rho_{d(l+1)} \leq f\left(\rho_{dl}, T\right), \quad \forall d, \quad l = c_e+1, c_e+2, \ldots, n_l - 2 \tag{C.18}$$

where the first layer is $c_e + 1$, and the last layer is $n_l - 2$ because the constant top layer is not included. Finally, in the additional face sheet plies below the core, the direction is reversed. Taking offset in Figure C.6 this corresponds to $\rho_{d2} \leq f\left(\rho_{d3}, T\right)$. In general this is written as:

$$\rho_{d(l-1)} \leq f\left(\rho_{dl}, T\right), \quad \forall d, \quad l = c_1 - 1, c_1 - 2, \ldots, 3 \tag{C.19}$$

where the first layer is $c_1 - 1$, and the last layer is 3 (defining the thickness constraint between layers 3 and 2), since the first ply is constant.

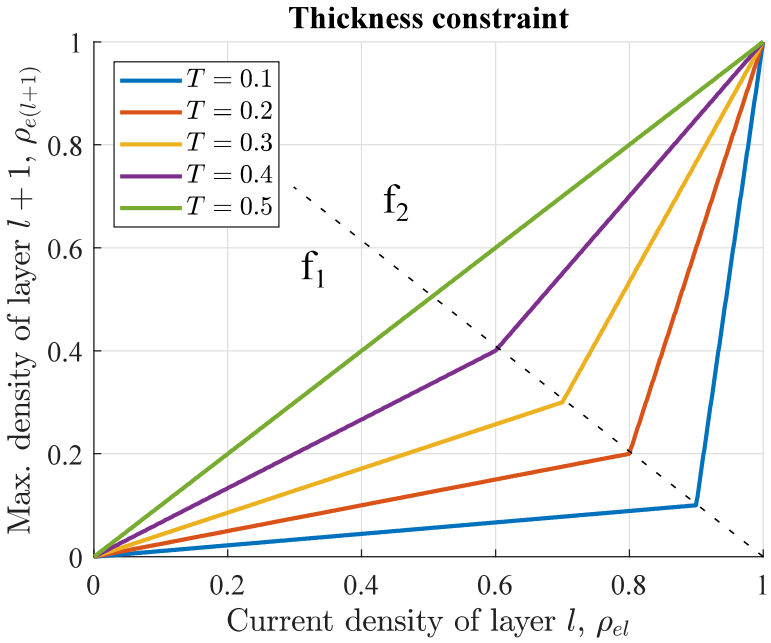

Fig. C.8: Plot of thickness constraint for different values of the T parameter. The thickness constraint uses the current density of layer l to determine the maximum density of the layer above $l+1$.

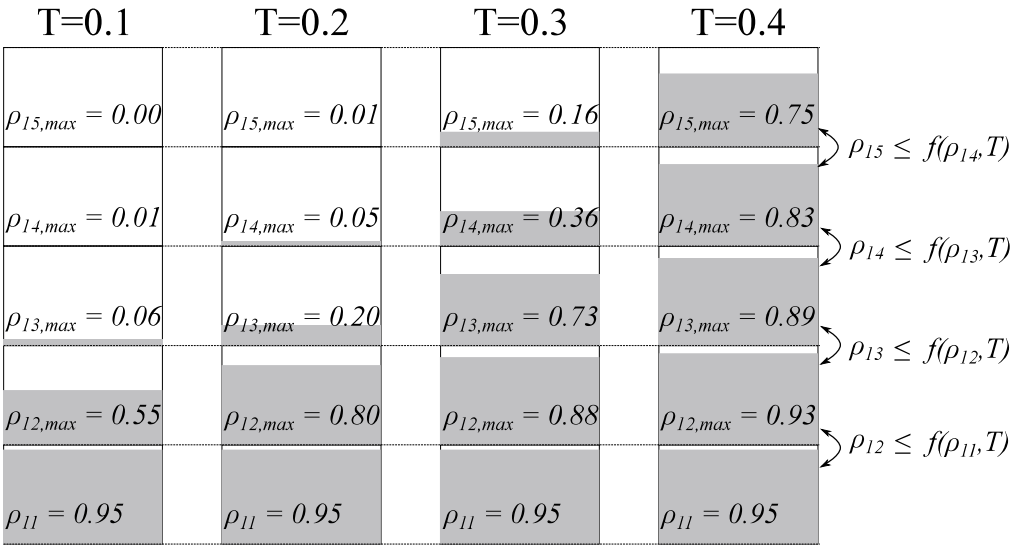

Fig. C.9: Visualization of the maximum allowable density in each of the five layers for different T values, when the first layer has a density of 0.95.

Symmetry

When the thickness constraints are defined separately for face sheets and core, it is straight forward to enforce symmetry of the face sheet layers around the core. This guarantees a symmetric lay-up if only one core material candidate is used. Symmetry is often important to uncouple the membrane and bending response which can cause warping during curing. A symmetric density in the face sheets in Figure C.6

corresponds to:

$$\rho_{11} = \rho_{18} \tag{C.20}$$
$$\rho_{12} = \rho_{17} \tag{C.21}$$
$$\rho_{13} = \rho_{16} \tag{C.22}$$

while symmetric material candidate choices similarly correspond to:

$$x_{11c} = x_{18c} \quad \forall c \tag{C.23}$$
$$x_{12c} = x_{17c} \quad \forall c \tag{C.24}$$
$$x_{13c} = x_{16c} \quad \forall c \tag{C.25}$$

Hence symmetry of face sheets can easily be included by a number of linear constraints. Another option is to let a design variable represent a bottom face sheet layer and its symmetric counterpart simultaneously, and thereby potentially halving the number of design variables. However, in this paper the former solution of using linear constraints is used due to being simpler to implement in the current framework.

Ply-drops

Another important manufacturing constraint is the ply-drop rate, sometimes measured as the tapering angle of the laminate, or simply the distance between subsequent ply-drops. Ply-drops lead to stress concentrations which follow from the sudden stiffness change and the resin rich triangular areas in the vicinity of the dropped plies. A minimum allowable distance between subsequent ply-drops hence ensures that the resulting stress concentrations do not influence each other. Dropping a balsa core ply yields a larger thickness change than dropping a face sheet layer, but in practice the balsa is usually machined to a triangular shape to reduce the resin pocket and thereby also the stress concentrations. In the following a face sheet or a core ply-drop are not distinguished.

Here the ply-drop rate is considered in terms of an allowable change in density from one domain to another as also done in Sørensen et al. (2014). The change in density from one domain to another corresponds to the number of plies being dropped, and given the dimensions of a domain it also implicitly corresponds to the distance between subsequent ply-drops (in an average sense if domains are larger than the minimum allowable distance between ply-drops). The change in density between two domains is simply the difference in the sum of densities. Hence if S is the maximum allowable number of plies that can be dropped from one domain to another, then the constraint can be formulated as:

$$-S \leq \sum_{l=1}^{n_l} \left(\rho_{dl} - \rho_{(d+1)l} \right) \leq S \tag{C.26}$$

where domain d and domain $d+1$ are adjacent domains.

C.3 Optimization approach

The gradient-based optimization approach is based on shell finite element models. Sensitivities are found in a semi-analytical manner, and the optimization problem is solved using sequential linear programming (SLP). The overall approach is visualized in the flowchart in Figure C.10. Details of the approach will be described in the following subsections. In general the approach is based on the implementations in Sørensen and Lund (2013); Sørensen et al. (2014); Sørensen and Lund (2015).

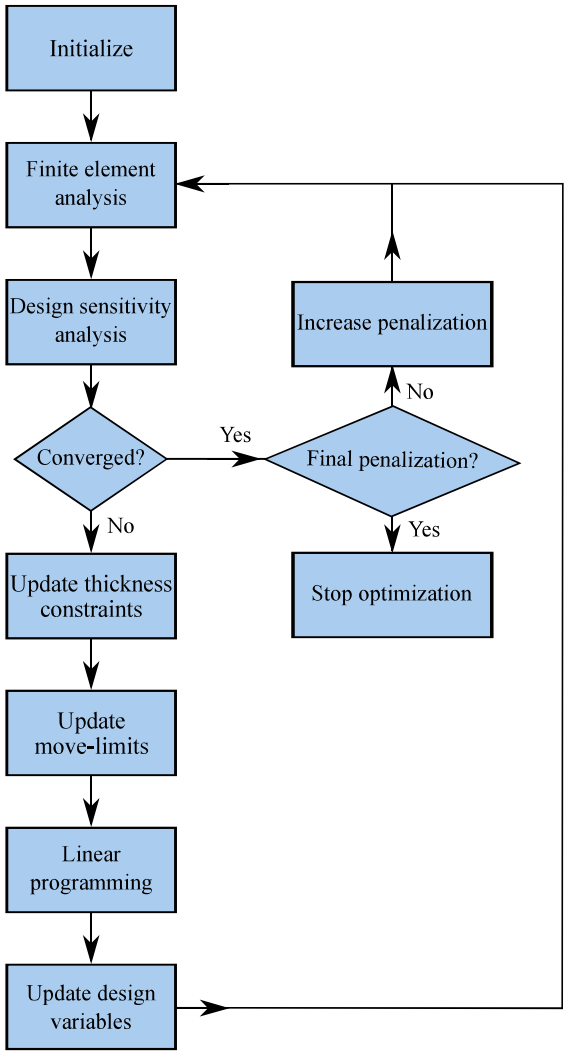

Fig. C.10: Flowchart of optimization approach.

C.3.1 Finite element analysis

The finite element analysis is based on equivalent single layer (ESL) shell elements. The shell elements use a 9-node isoparametric formulation as in Panda and Natarajan (1981). The shell element is implemented in the in-house research code referred to as the MUltidisciplinary Synthesis Tool MUST (2018). In the finite element method the

discretized static equilibrium is written as:

$$\mathbf{KD} = \mathbf{F} \tag{C.27}$$

where $\mathbf{F}$ is the global force vector, $\mathbf{K}$ is the global stiffness matrix, and $\mathbf{D}$ is the global displacement vector. The global stiffness matrix is assembled from element stiffness matrices. The element stiffness matrix of element e can be written as:

$$\mathbf{K}_e = \sum_{l=1}^{n_l} \int_V (\mathbf{B}_{el})^T \mathbf{E}_{el} \mathbf{B}_{el} dV \tag{C.28}$$

where $\mathbf{B}_{el}$ is the strain-displacement matrix and $\mathbf{E}_{el}$ is the constitutive matrix.

Buckling load factors λ_j can be found by solving the linear eigenvalue buckling problem given as:

$$\left(\mathbf{K} + \lambda_j \mathbf{K}_\sigma\right) \mathbf{\Phi}_j = \mathbf{0}, \quad j = 1, 2, \ldots \tag{C.29}$$

where $\mathbf{\Phi}$ is the mode shape associated with buckling load factor λ_j, and $\mathbf{K}_\sigma$ is the global stress stiffness matrix. The global stress stiffness matrix is assembled from element stress stiffness matrices given as:

$$\mathbf{K}_{\sigma,e} = \sum_{l=1}^{n_l} \int_V (\mathbf{G}_{el})^T \mathbf{S}_{el} \mathbf{G}_{el} dV \tag{C.30}$$

where $\mathbf{G}_{el}$ is a matrix containing derivatives of shape functions and $\mathbf{S}_{el}$ is a matrix containing layer stresses.

C.3.2 Design sensitivity analysis

Design sensitivities are found using the semi-analytical direct differentiation approach. In the direct differentiation approach the sensitivities of the displacements $\mathbf{D}$ are found by differentiating the discretized static equilibrium in (C.27). If z_i is a generic design variable this can be written as:

$$\mathbf{K} \frac{d\mathbf{D}}{dz_i} = -\frac{\partial \mathbf{K}}{\partial z_i} \mathbf{D} + \frac{\partial \mathbf{F}}{\partial z_i} \tag{C.31}$$

where the right-hand side is usually called the pseudo load vector. In this paper the external loads $\mathbf{F}$ are considered independent of the design variables, and hence the last term vanishes. The approach is semi-analytical meaning that the partial derivative of the global stiffness matrix is based on finite difference calculations of the element stiffness matrices. Furthermore, the sensitivity of buckling load factors depends on the partial derivative of the global stress stiffness matrix, which is also based on finite difference calculations of element stress stiffness matrices. See, for example, Lund (2009) for more details on buckling load factor sensitivities.

C.3.3 Optimization

Sequential linear programming is used to optimize the problem. In this approach the problem is linearized with respect to the design variables, and linear programming is used to find the change in design variables that minimizes the objective while satisfying the linearized constraints. This is done sequentially until convergence is achieved. The linear programming problem is solved using the Sparse Nonlinear Optimizer SNOPTA by Gill et al. (2005).

Adaptive move-limits and merit function approach

Since the linearization is only valid for small changes in design variables, move-limits are used to control the allowable changes. To help convergence adaptive move-limits combined with a merit function approach is used, see Sørensen and Lund (2015) for details. The merit function ensures the feasibility of the problem by penalizing the objective function depending on the infeasibility. Adaptive move-limits are used to tighten the move-limits if the merit function oscillates.

Penalization and continuation approach

Penalization is used to favor discrete design variables. However, if high penalization powers are applied early in the optimization, it is likely to end up in a sub-optimal local optimum. To find a strong local optimum a continuation approach is used. In the continuation approach penalization factors are increased in steps. In this paper the penalization factors are increased whenever convergence is achieved with current penalization. Penalization powers for both candidate materials, p, and density q, are used in the following steps:

$$p = \{1, 4, 20\} \tag{C.32}$$

$$q = \{0, 4, 20\} \tag{C.33}$$

Convergence

Convergence of the optimization is defined in terms of a relative change of the merit function. The relative change in merit function can be written as:

$$\left\| \frac{\Phi_k - \Phi_{k-1}}{\Phi_{k-1}} \right\| < \text{tol} \tag{C.34}$$

where Φ_k is the merit function in iteration k and tol is the convergence tolerance. Whenever convergence is achieved, penalization powers are increased. When convergence is achieved with the final penalization powers the optimization is terminated. In general a convergence tolerance of 10^{-2} is used in the examples. Furthermore, termination is only allowed if the maximum infeasibility is less than a given tolerance (here taken to 1%).

Measures of non-discreteness

Measures of non-discreteness are introduced to quantify the non-discreteness of design variables. A measure of 0% means that all design variables are fully discrete (either 0 or 1), while 100% non-discreteness means that all design variables are 0.5. The measure of density non-discreteness, M_{dnd}, is based on the one used in Sigmund (2007), and is given as:

$$M_{dnd} = \frac{4\sum_{e,l} V_{el}\rho_{el}(1-\rho_{el})}{\sum_{e,l} V_{el}} 100\% \tag{C.35}$$

The measure of candidate non-discreteness, M_{cnd}, is taken from Sørensen et al. (2014) as:

$$M_{cnd} = \frac{\sum_{e,l} V_{el}\rho_{el}^2 \prod_{c=1}^{n_c} \left(\frac{1-x_{plc}}{1-\frac{1}{n_c}}\right)^2}{\sum_{e,l} V_{el}\rho_{el}} 100\% \tag{C.36}$$

C.4 Numerical examples and results

Three numerical examples will demonstrate the application of DMTO for sandwich structures. All examples use the material properties listed in Table C.1. The GFRP UD values are taken from Sørensen et al. (2014) and correspond to typical material values for epoxy infused GFRP with a fiber volume fraction of 50 %. In this table GFRP biax corresponds to the equivalent properties of a $\pm 45^\circ$ laminate based on the GFRP UD properties. The GFRP biax material will in the following sections simply be referred to as biax.

The results obtained will depend on the initial design variables, and it is important not to favor a particular candidate material in advance. Initial candidate design variables are equally distributed such that each candidate will have the same initial material weight. Moreover, all examples are started from a full density configuration. The finite element analysis for all presented examples is based on equivalent single layer (ESL) shell elements, however the new DMTO thickness parameterization has also been implemented for solid shell elements, see Sjølund et al. (2018).

No detailed mesh convergence study is included, but it is checked that doubling the number of elements in example 2 only increases the tip displacement by 0.16 % and the first buckling load factor by 0.09 %, while for example 3, quadrupling the number of elements (halving element edge length) increases the tip displacement by 1.32 %, and the first buckling load factor by 2.51 %. These mesh sensitivities are calculated based on initial models. However, in general the results are relatively mesh insensitive due to the patch/domain parameterization.

All numerical examples have been run on a 24 core Intel Xeon i5 workstation running at 3 GHz. Most time is spent on sensitivity analysis which is very parallelizable, and hence more complicated structures can be optimized given more computational resources or time. The number of design variables in the three examples are 28, 434, and 2672, respectively.

Property	GFRP UD	GFRP biax	Balsa	Units
E_{11}	34.00	13.09	0.21	GPa
E_{22}	8.20	13.09	0.21	GPa
E_{33}	8.20	8.20	6.84	GPa
G_{12}	4.50	9.55	0.08	GPa
G_{13}	4.50	3.52	0.24	GPa
G_{23}	4.00	3.52	0.24	GPa
ϱ	1910	1910	220	kg/m^3
ν_{12}	0.29	0.45	0.23	-
ν_{13}	0.29	0.29	0.01	-
ν_{23}	0.29	0.29	0.01	-
t	1.00	1.00	6.35	mm

Table C.1: GFRP material properties used in all examples.

C.4.1 Example 1

In this example the mass of a simply supported (SS) square plate is minimized while subject to both compliance and buckling constraints. The plate is loaded by a resulting compressive force of 20 kN distributed on the right edge. The boundary conditions and dimensions can be seen in Figure C.11. The figure also shows the used 12x12 finite element discretization. All elements are grouped together into one material candidate patch and one density domain, resulting in a relatively simple constant stiffness plate. The problem is solved with 20% initial move-limits and thickness constraints with the T-parameter in (C.16) of $T = 0.3$.

The lay-up including possible material candidates is given in Table C.2. The outer layers (1 and 8) have fixed full density, while the density of the remaining layers is free to vary. The biax candidate corresponds to biaxial angle ply of $\pm 45°$. Elastic properties are listed in Table C.1. In order to assess the influence of each of the constraints the optimization is performed in three cases:

- Minimize mass with constraint on compliance
- Minimize mass with constraint on buckling
- Minimize mass with both constraints

Layer(s)	Thickness	Candidate(s)	Density
1	1 mm	UD/0°, UD/90°, biax	Fixed
2-3	1 mm	UD/0°, UD/90°, biax	Free
4-5	6.35 mm	Balsa	Free
6-7	1 mm	UD/0°, UD/90°, biax	Free
8	1 mm	UD/0°, UD/90°, biax	Fixed

Table C.2: Lay-up and material candidates.

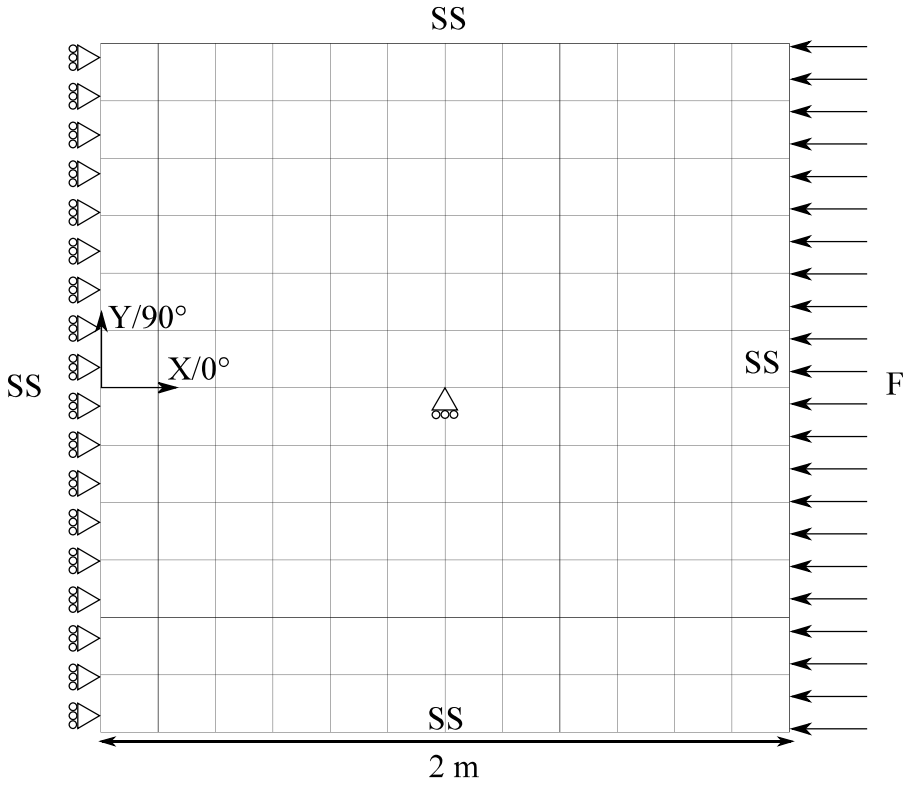

Fig. C.11: Finite element mesh and boundary conditions of the square plate used in example 1. All edges are simply supported (SS), the left edge is also supported in the X-direction, and the center node is constrained in the Y-direction to prevent rigid body displacements.

Results

In the first case the mass is minimized with the compliance constrained to be less than 4.15 J. This compliance corresponds to a maximum edge x-displacement of approximately 0.21 mm. The result is visualized in 3D with layer thicknesses scaled by 20 in Figure C.12. The result uses four UD/0° layers and zero balsa core layers. This is to be expected as the stiffness/weight ratio favors UD/0° compared to balsa and other candidates. The optimized result can also be found in the first column of Table C.3. Here grey cells indicate zero density. Note that a subsequent buckling analysis of this design reveals a low buckling load factor of 0.031.

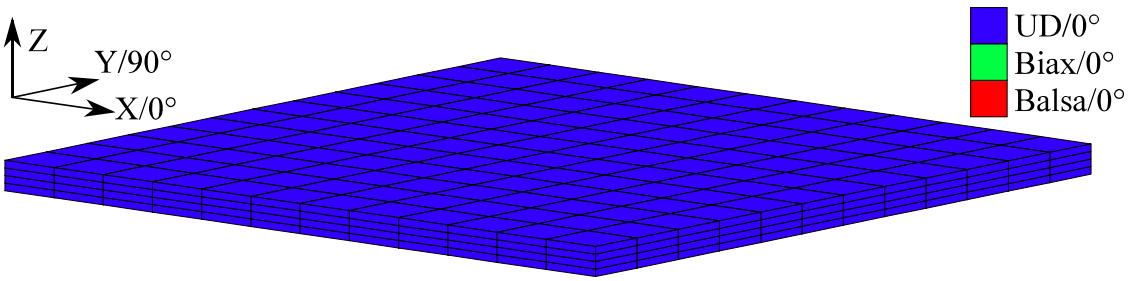

Fig. C.12: 3D visualization of the compliance constrained result with layer thicknesses scaled by a factor of 20.

In the second case the mass is minimized with a constraint on the minimum buckling load factor to be larger than 4.10. The optimized result is shown in Figure C.13, and listed in the second column of Table C.3. Here the maximum number of balsa layers are naturally present since it is a weight efficient way to increase the bending stiffness. Furthermore, biax is preferred in four face sheet layers over UD/0° and UD/90°. However, while the buckling load factor is much higher than in case 1, the stiffness is also lower (compliance is increased).

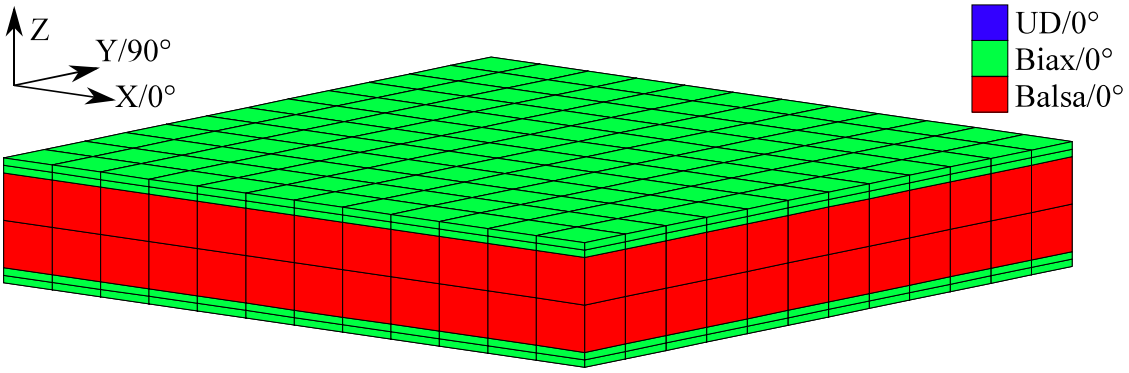

Fig. C.13: 3D visualization of the buckling constrained result with layer thicknesses scaled by a factor of 20.

In the third case constraints on both compliance and buckling are imposed. As can be seen in Figure C.14 a compromise is achieved. The compromise contains two UD/0° layers for sufficient longitudinal stiffness while two balsa and two biax layers are chosen for sufficient buckling strength. The weight is only slightly larger than in case 2, due to requiring 100% density in layers 3 and 6 rather than 99%.

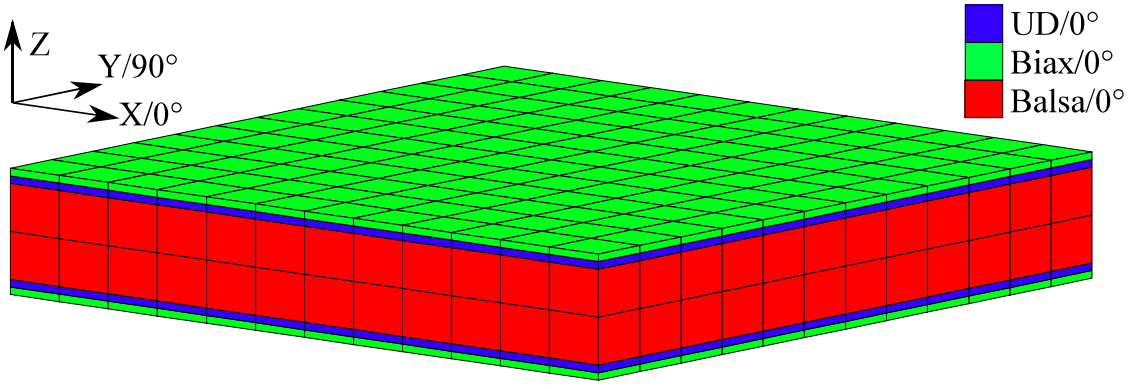

Fig. C.14: 3D visualization of the combined result with layer thicknesses scaled by a factor of 20.

Comparison of results

The result in the compliance constrained case is very intuitive as UD/0° has the highest specific stiffness, and no bending stiffness is needed. Layers 3 and 6 only reach a density of 94%, since this is sufficient to satisfy the compliance constraint. However, with increased penalization these layers can be brought closer to 100%.

The buckling result is also somewhat intuitive. The maximum number of balsa layers are used to provide bending stiffness in a weight efficient manner. The face sheet layers are chosen as biax ($\pm 45^\circ$). A density of 99% of layers 3 and 6 is needed to satisfy the buckling constraint. To compare the influence of biax layers compared to UD/0°, it is possible to evaluate the same density configuration, but replacing biax with UD/0°. This yields a buckling load factor of 3.17, i.e. significantly lower than 4.10.

This can also be used to explain the little mass difference in the combined case. The external layers (1 and 8) are the most important layers with regard to bending stiffness. Changing these layers to biax almost brings the buckling load factor from 3.17 to 4.10. Changing the density of the UD/0° layers 3 and 6 from 99% to 100% is thereby enough to satisfy the constraint. This one percent density change also corresponds to the increase in mass. However, note that the one percent increase in density corresponds to a higher increase in stiffness due to penalization.

	Compliance $C < 4.15$		Buckling $\lambda > 4.10$		Combined Both	
Layer(s)	Dens.	Cand.	Dens.	Cand.	Dens.	Cand.
1	100%	UD/0°	100%	Biax	100%	Biax
2	0%	UD/0°	0%	Biax	0%	UD/0°
3	94%	UD/0°	99%	Biax	100%	UD/0°
4	0%	Balsa	100%	Balsa	100%	Balsa
5	0%	Balsa	100%	Balsa	100%	Balsa
6	94%	UD/0°	99%	Biax	100%	UD/0°
7	0%	UD/0°	0%	Biax	0%	UD/0°
8	100%	UD/0°	100%	Biax	100%	Biax
Mass		29.61		41.69		41.82
Compliance		4.15		(7.91)		4.15
Buckling		(0.031)		4.10		4.11
M_{dnd}		2.50 %		0.41 %		0.06 %
M_{cnd}		0.0 %		0.0 %		0.0 %

Table C.3: Minimization of mass of plate subject to a compliance constraint, a buckling constraint, and both constraints simultaneously. Grey cells indicate zero density.

C.4.2 Example 2

In the next example the mass of a closed cylinder is minimized while subject to displacement and buckling constraints. The finite element model, dimensions and boundary conditions can be seen in Figure C.15. The cylinder is divided into 20 density domains, while all elements are included in one material patch. The cylinder is manufactured in an external single sided mold, and hence the outer geometry is constant. Therefore, during optimization, material is removed from the inside. This corresponds to an offset material removal during optimization which is achieved us-

ing the dummy layer approach. The problem is solved with 15% initial move-limits and thickness constraints (C.16) use $T = 0.3$. The allowable density change between adjacent domains is set to $S = 2$ corresponding to a maximum of a single ply-drop in both face sheets (due to symmetry) or two ply-drops in the core.

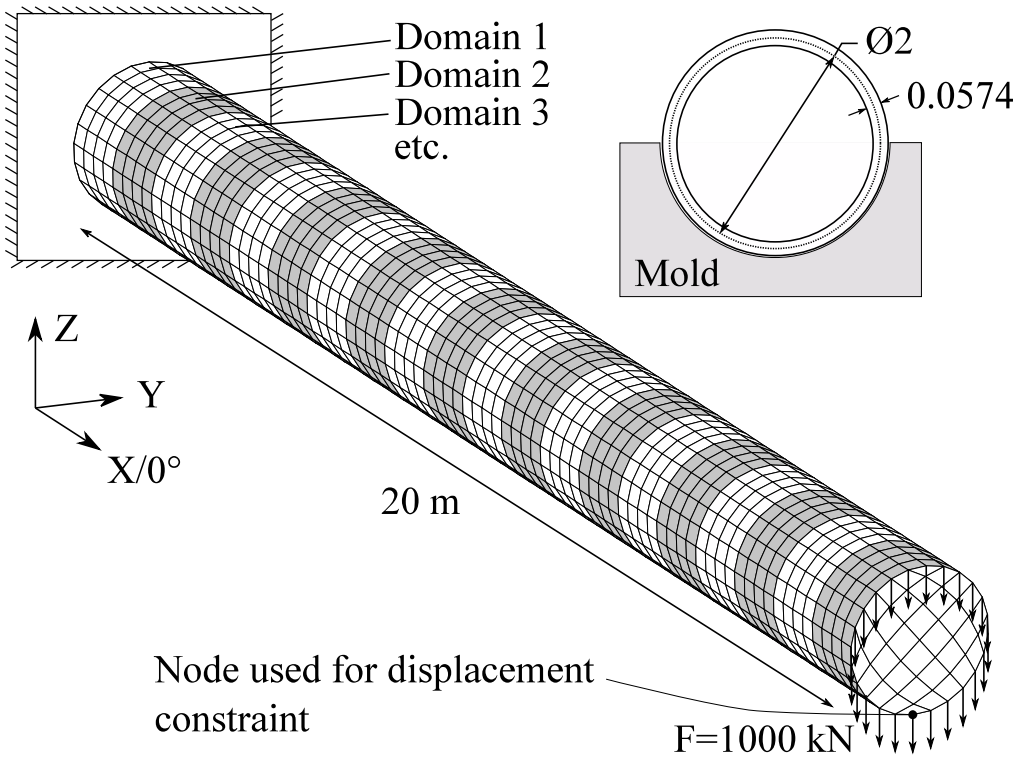

Fig. C.15: Finite element model, boundary conditions, and domains of the cylinder used for example 2.

The lay-up including material candidates can be seen in Table C.4. The external layers have fixed full density with biax as the only material candidate. The other face sheet layers have free density and two material candidates in UD/0° and biax while core layers are balsa. The full density thickness is 57.4 mm as shown in Figure C.15, but it may be changed during optimization in each of the domains. To reduce the number of design variables, face sheet layers are taken to have a ply thickness of 2 mm rather than 1 mm. Again the minimization of mass is performed in three cases:

Layer(s)	Thickness	Candidate(s)	Density
1	2.0 mm	Biax	Fixed
2-8	2.0 mm	UD/0°, biax	Free
9-12	6.35 mm	Balsa	Free
13-19	2.0 mm	UD/0°, biax	Free
20	2.0 mm	Biax	Fixed

Table C.4: Lay-up and material candidates.

- Minimize mass with constraint on end displacement
- Minimize mass with constraint on buckling
- Minimize mass with both constraints

Results

The resulting lay-up from the case with only a displacement constraint can be seen in Figure C.16 while results are listed in Table C.5. Both the thickness distribution and choice of candidates are as expected. Most material is placed towards the constrained end, and UD/0° is chosen for the maximum bending stiffness. However, it is interesting to note that all sandwich layers have been removed. This is because sandwich layers will push the internal face sheet layers inward (due to the fixed outer geometry) and thereby lower the area moment of inertia of the cross section.

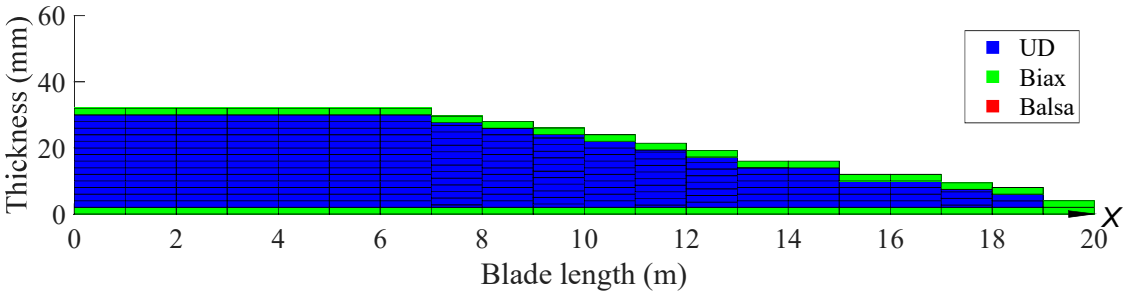

Fig. C.16: Cylinder lay-up resulting from mass minimization with a displacement constraint. The X-axis corresponds to the outer surface of the cylinder.

Next, the lay-up from the case with only a buckling constraint can be seen in Figure C.17. Here the maximum amount of four balsa layers is used from 0-14 m. The face sheet layers are dominated by biax candidates, although, perhaps surprisingly, there are also three layers of UD/0°. However, the UD/0° layers are the first to be dropped, and one of these layers in fact only exists in a single domain. As a check the optimized density configuration can be evaluated with only biax or UD candidates available in the face sheets. Only having biax candidates yields a buckling load factor of 3.16, while only having UD candidates yields a buckling load factor of 2.53. The lack of UD/0° layers in the optimized design also results in a very compliant design with a tip displacement of 2.15 m as can be seen in Table C.5. Utilizing the balsa layers yields a high local bending stiffness. By inspection all buckling modes involve local bending, similar to the mode shown in Figure C.19, and hence the usage of balsa makes good sense. Actually the optimized design is slightly infeasible with a buckling load factor of 3.49. This is because an infeasibility tolerance of 1% is used.

Finally, the mass is minimized with both displacement and buckling constraints. The resulting lay-up can be seen in Figure C.18. Again the result is strictly speaking infeasible, but within the infeasibility tolerance of 1%. It can be seen that UD/0° layers are used to achieve sufficient longitudinal stiffness (to satisfy the tip displacement constraint) while balsa layers are added to provide sufficient local bending stiffness to satisfy the buckling constraint. However, the UD/0° layers of course also contribute

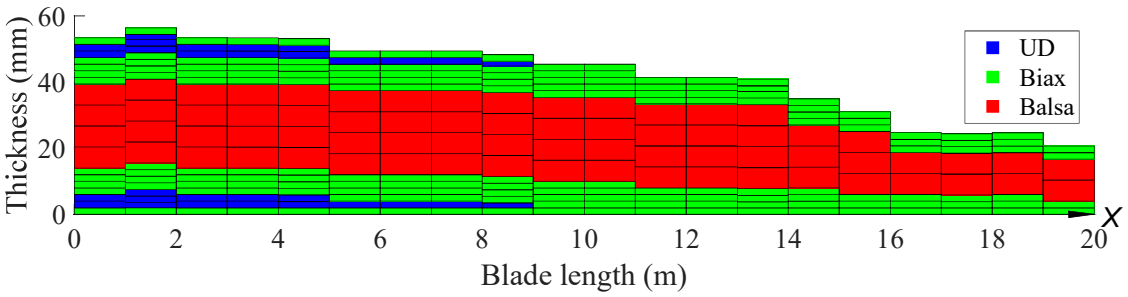

Fig. C.17: Cylinder lay-up resulting from mass minimization with a buckling constraint. The X-axis corresponds to the outer surface of the cylinder.

to the local bending stiffness. In fact, the maximum number of balsa layers is only utilized in a single domain, from 1-2 m.

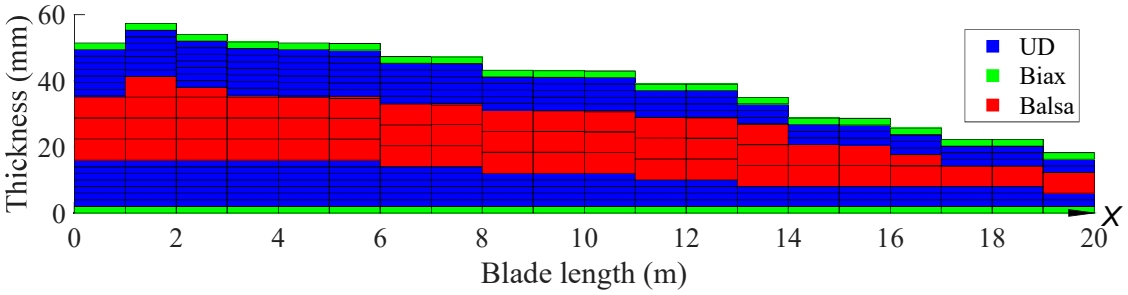

Fig. C.18: Mass minimization of cylinder with both compliance and buckling constraints. The X-axis corresponds to the outer surface of the cylinder.

	Displacement $u_y < 1.0$	Buckling $\lambda > 3.5$	Combined Both
Mass	5731	5719	6418
Displacement	1.00	(2.15)	1.00
Buckling	(0.88)	3.49	3.48
M_{dnd}	0.91 %	0.92 %	3.34 %
M_{cnd}	0.0 %	0.0 %	0.0 %

Table C.5: Minimization of mass of a cylinder subject to a displacement constraint, a buckling constraint, and both constraints simultaneously.

Comparison of results

For the case with only a displacement constraint all core layers are removed, thereby creating a monolithic laminate. In this case as much material as possible is placed near the fixed end, and from 0-7 m the maximum number of face sheet layers is utilized.

For the case with only a buckling constraint the thickness distribution is slightly different as the peak thickness is located between 1-2 m. This is due to the fixed end

preventing buckling mode shapes in its vicinity, and thus the maximum thickness location is pushed slightly outwards. This is visualized in Figure C.19, where a mode shape with peak displacement at 1.5 m is seen. This mode shape is taken from the optimized model constrained only in buckling.

In the case with both displacement and buckling constraints it seems that the best compromise is to add balsa layers for local bending stiffness and UD face sheet layers for longitudinal stiffness. Adding balsa layers reduce the area moment of inertia of the cross section which means that more UD/0° layers must be added to satisfy the displacement constraint which in turn increases the mass of the cylinder significantly.

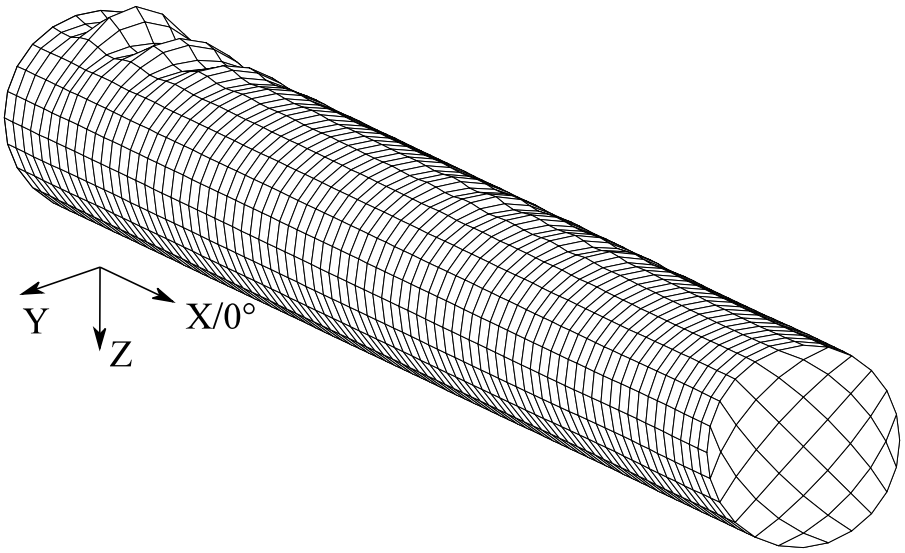

Fig. C.19: A buckling mode shape with the peak displacement near the constrained end from the optimization with only a buckling constraint.

C.4.3 Example 3

In the third and last example the mass of a wind turbine blade main spar is minimized. The main spar is similar to the one used in Lund et al. (2008) and Sørensen et al. (2014). The blade is subject to a displacement constraint in load case 1 (LC1) of $u_y < 1.0$ m, and buckling constraints in two load cases LC1 and LC2, both being $\lambda > 6$. The blade is loaded with a distributed load of 164.7 kN as shown in Figure C.20 which corresponds to LC1, while LC2 is the same load case but with reversed sign. The blade is 14 m in length and is divided into 120 domains where the density can vary independently (but limited by the ply-drop constraints). These domains along with mesh and root dimensions are also shown in Figure C.20. Furthermore, the main spar is divided into 8 material candidate patches as shown in Figure C.21. Within a patch the choice of candidate material in a given layer is the same for all elements.

The problem is solved with $T = 0.3$, move-limits of 10%, and an allowable density change between each domain of $S = 2$. The lay-up is given in Table C.6 and is the same as in example 2.

Layer(s)	Thickness	Candidate(s)	Density
1	2.0 mm	Biax	Fixed
2-8	2.0 mm	UD/0°, biax	Free
9-12	6.35 mm	Balsa	Free
13-19	2.0 mm	UD/0°, biax	Free
20	2.0 mm	Biax	Fixed

Table C.6: Lay-up and material candidates.

Results (default)

In this example the main spar is optimized with all criteria acting simultaneously. Results from the optimization are listed in Table C.7 (column 'Default'), and the resulting lay-up in the 8 patches are shown in Figure C.22. In the spar caps, the peak thicknesses of the face sheets are not located at the root, but rather at 9 m from the root as marked with the blue stars. This is because, unlike the cylinder, the wind turbine main spar has a varying cross section resulting in a varying ratio between the bending moment and area moment of inertia. Due to the high requirements on buckling load factors ($\lambda > 6$), balsa is also used in the spar caps. In fact, the maximum amount of four balsa plates are used around 4-5 m from the root in both spar caps. In Figure C.22 the small numbers above the lay-up show the density sum of each domain. It can be seen that in the spar cap domains close to the tip, the maximum allowable change in density of $S = 2$ is utilized.

The resulting lay-up of the corner patches is non-smooth in the sense that many thickness jumps can be seen. The thickness jumps are due to balsa being favored in some positions while an additional face sheet ply is favored other places. In general,

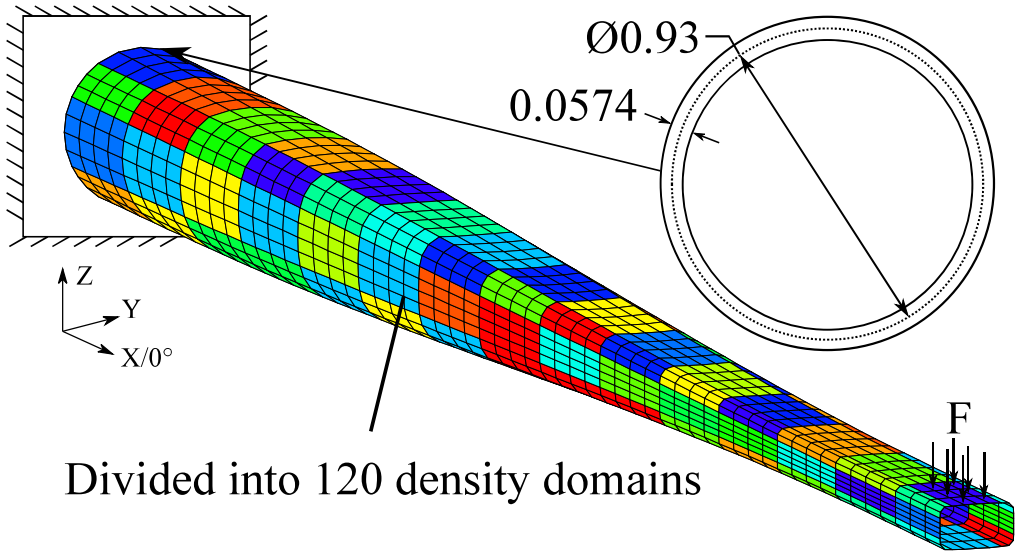

Fig. C.20: The wind turbine main spar is divided into 120 domains. In each domain the densities can change independently, only limited by constraints on the allowable density change. Also shown is the dimensions of the root end.

	Default	Variable peak	Root peak
Mass	1427	1433	1465
Displacement LC1	1.00	1.00	1.00
Buckling LC1	5.99	5.99	6.00
Buckling LC2	5.99	5.99	5.99
M_{dnd}	6.53 %	5.69%	7.90%
M_{cnd}	0.00 %	0.00%	0.00%

Table C.7: Minimization of mass of a wind turbine main spar subject to displacement and buckling constraints.

a trend of multiple balsa layers near or in the tip can be seen, which is due to the presence of local buckling modes near the load application as shown in Figure C.23.

The webs utilize the maximum number of balsa layers throughout most of the length. However, as no edgewise load cases are included, the webs are not very heavily loaded. In fact, the maximum allowable density change of two between web domains and adjacent corner domains is utilized everywhere to remove as much material as possible in the webs. Because this constraint prohibit any more material removal, the maximum number of balsa layers are utilized since they weigh less than GFRP candidates.

The main issue with the optimized result is that it is not desirable to manufacture because of the many thickness jumps and sudden increase in balsa thickness towards the tip. This is in spite of ply-drop constraints which limit the change in density between adjacent domains.

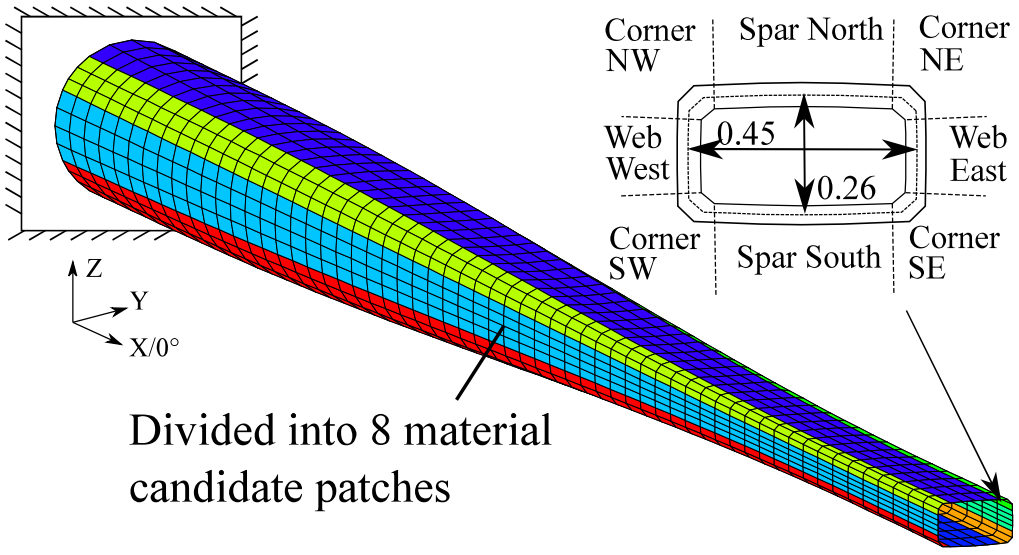

Fig. C.21: The wind turbine main spar is divided into 8 patches. In each patch different candidate materials can be chosen for each of the face sheet layers. The dimensions of the tip and the naming of the 8 patches are given.

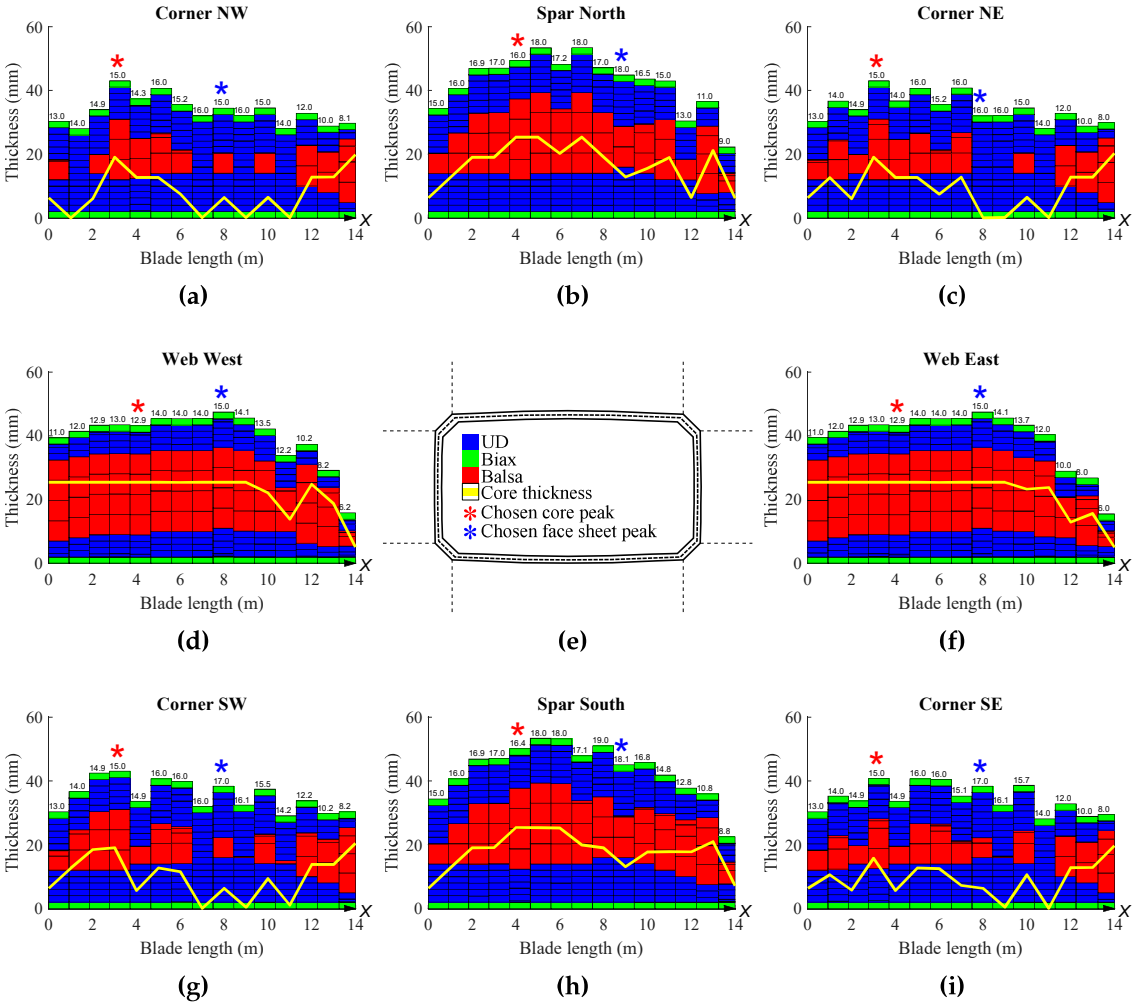

Fig. C.22: Thickness distribution and candidate choices of each of the 8 patches of the wind turbine main spar. The 8 patches are also visualized in Figure C.21. The numbers above each domain is the density sum of that domain. The red and blue stars denote the chosen peak thicknesses of balsa and face sheets.

Results (variable peak)

To ensure a manufacturable result, a two-stage approach is suggested. In this approach a subsequent optimization is performed based on the results from the first optimization. However, in the subsequent optimization, peak thickness constraints are added to the problem. Peak thickness constraints define a peak thickness in the length direction for both face sheets and core for each of the eight patches. In adjacent domains on either side of the peak, the density sum must be equal to or smaller than at the peak as shown in Figure C.24. The chosen thickness peaks are displayed with red and blue stars in Figure C.22 for balsa and face sheets, respectively. Each of the four corner patches have their peak number of face sheet layers in different positions, in either domain 8, 9, or 10 (when counting from $X = 0$). For simplicity, the face sheet peak is chosen to be domain 9 for all corners. The core peaks are chosen to domain

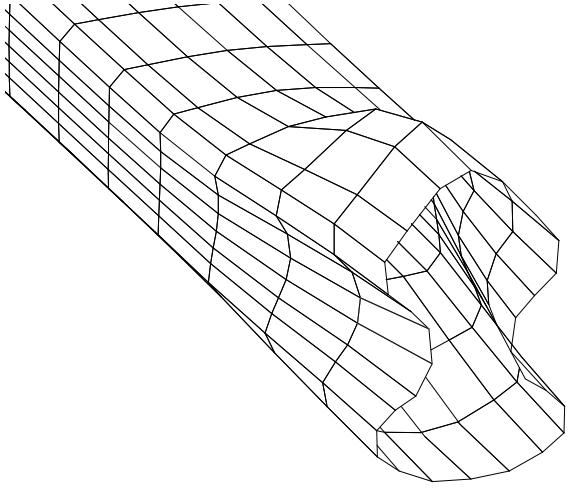

Fig. C.23: Local buckling mode near the load application at the tip.

4 for all corners, ignoring the thick core domains near the tip as this is not ideal for manufacturing. The webs have multiple domains with the maximum number of balsa layers. Here domain 5 is chosen as core peak for both webs, as this is located in the middle among the maximum core thickness domains. In a similar manner domain 5 is chosen as the balsa peak for both spar caps. When the peak thickness constraints have been added, the optimization is started from a full density configuration as in the first run.

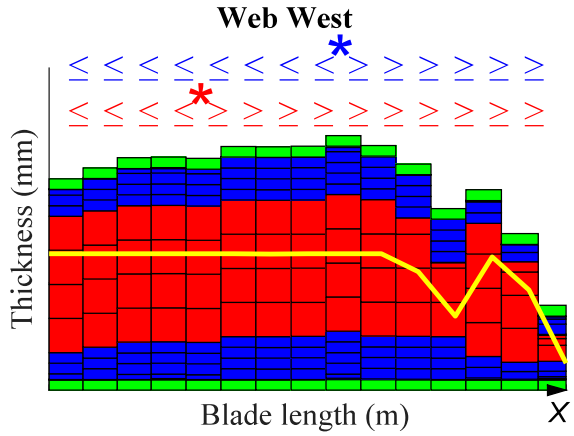

Fig. C.24: Illustration of the peak thickness constraints used in a subsequent optimization. In the subsequent optimization the density sum of balsa and face sheets must be decreasing on either side of their respective peaks, marked with stars. The peak balsa thickness is chosen to be in the center among the maximum core thickness domains.

Results from the subsequent optimization with peak thicknesses constrained is shown in Figure C.25, and results are listed Table C.7 in column 'Variable peak'. It can be seen that the thickness distributions are much smoother, and that the resulting lay-up is much easier to manufacture. There is a slight increase in mass as expected, but the increase is only 6 kg (0.42%).

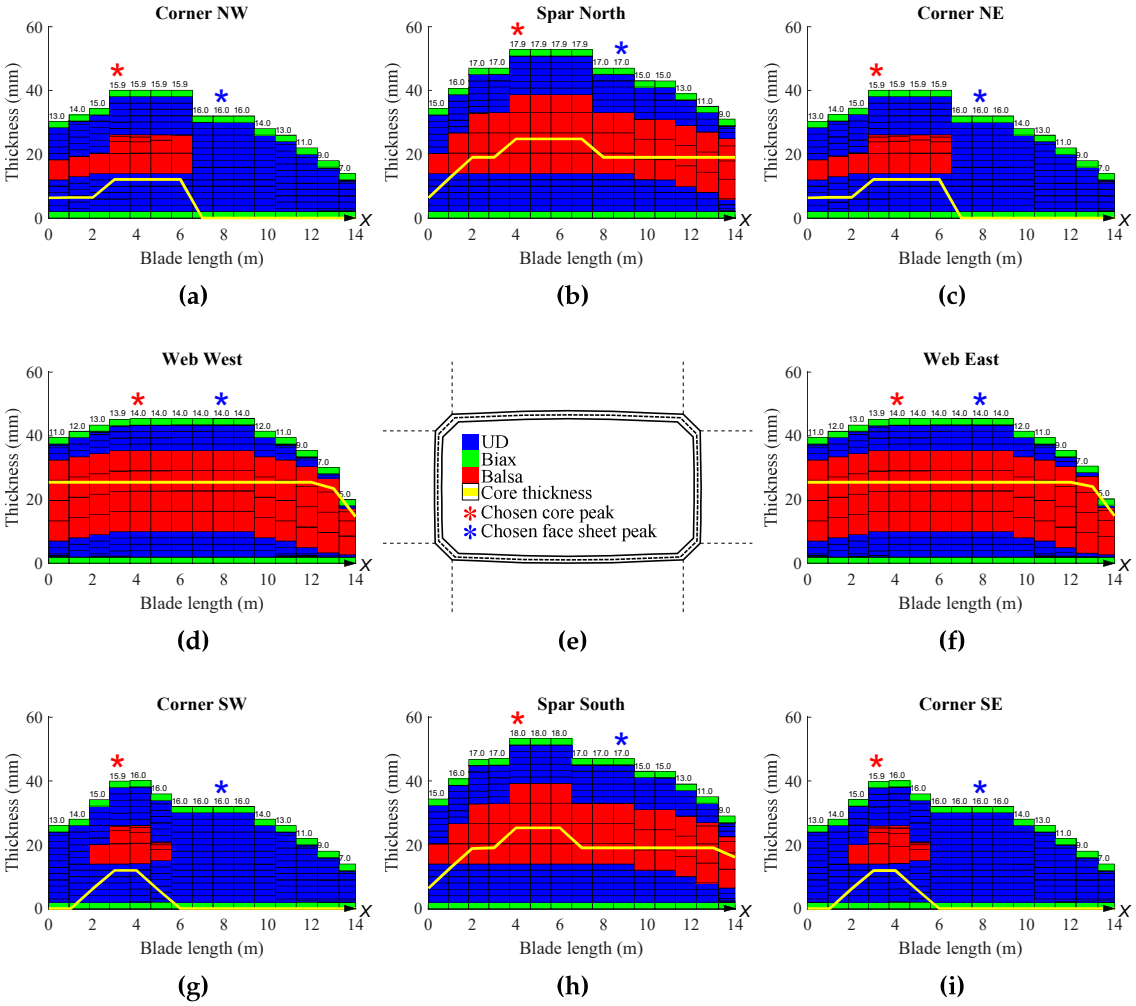

Fig. C.25: Optimization re-run of the default results shown in Figure C.22. In this re-run peak thicknesses have been enforced such that on either side of the peak thickness the density sum must decrease. Peak thicknesses are defined for both balsa and facesheets as shown with red and blue stars respectively.

Results (root peak)

Another approach which can be enforced from the start, is to again add peak thickness constraints, but with all peaks located at the root. Results obtained from this approach are shown in Figure C.26, and are listed in Table C.7 in column 'Root peak'. Again, the obtained results are much more manufacturable than initial results because of a smoother thickness distribution and because no plies are started/stopped multiple times. However, this simplified approach of enforcing the peak thickness at the root comes with a larger penalty on the mass as the optimized result in this case is 38 kg (2.7%) heavier than the default result. The main advantage is that it can be enforced from the beginning, and hence it does not rely on a subsequent optimization.

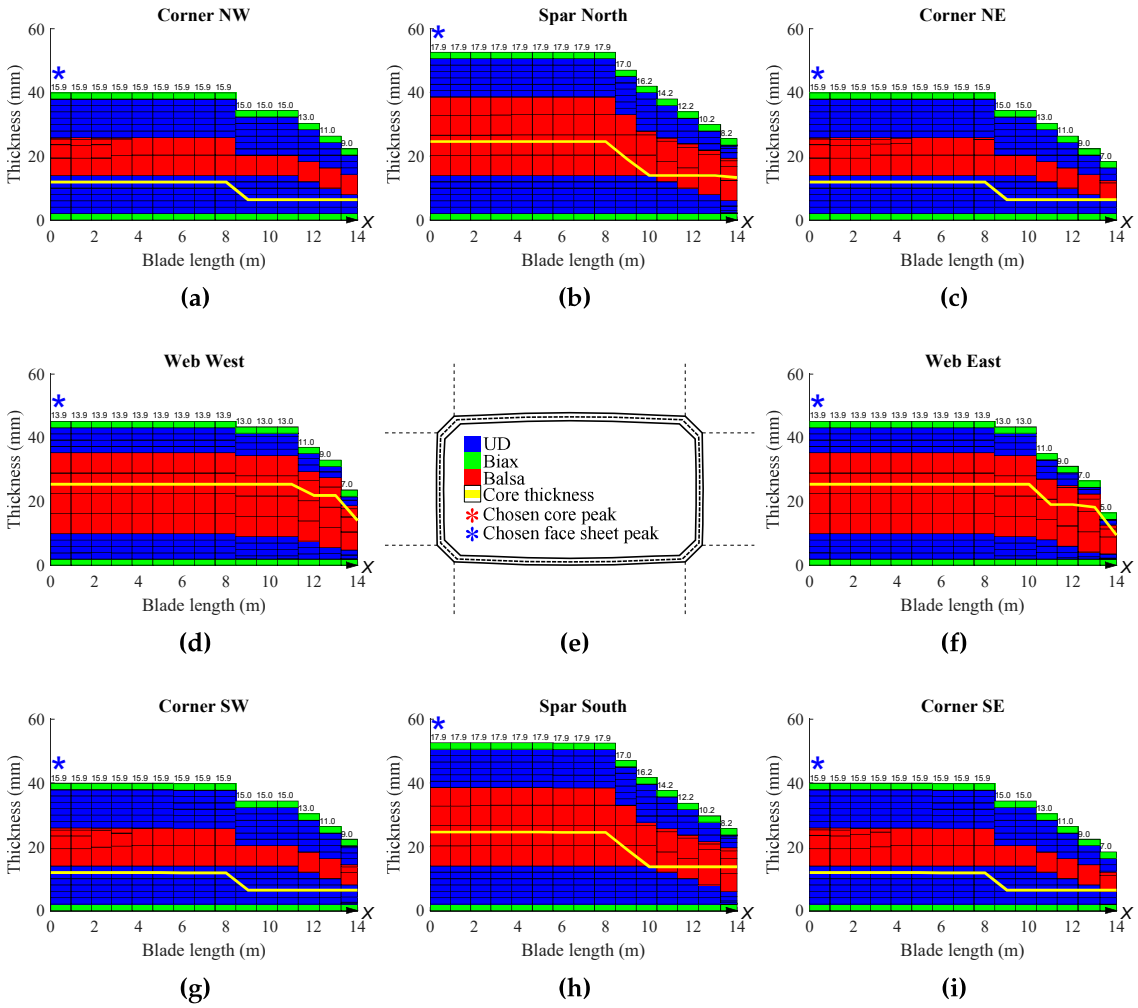

Fig. C.26: Optimization with all peak thicknesses located in the root end.

C.5 Conclusion

In this paper the Discrete Material and Thickness Optimization (DMTO) method has been applied for structural optimization of composite sandwich structures. The goal of using DMTO for sandwich structures is to, throughout a structure, determine both the integer number of face sheet layers, the fiber angle (from a number of candidates) for each face sheet layer, and the core thickness while minimizing the mass using gradient-based optimization. Here balsa is used as core material, and the thickness is also discrete in the sense that only a finite number of balsa plate thicknesses are available.

Using a new thickness parameterization that links density design variables to ply thicknesses rather than constitutive properties, it is possible to size sandwich core and face sheet layers simultaneously without introducing intermediate voids. This allows core layers to always be positioned in the middle of the laminate, and to always be covered by at least one face sheet ply. By separating core and face sheet layers it is also

possible to use different ply thicknesses (for example, balsa plates are much thicker than GFRP plies). Furthermore, it is possible to enforce symmetry of the face sheets around the core.

The approach is demonstrated on three numerical examples: a simple constant stiffness plate, a variable thickness cylinder, and finally a wind turbine spar. In all cases the mass is minimized while considering compliance (displacement) and buckling constraints. Moreover, manufacturability of the wind turbine main spar is discussed and it is shown how peak thickness constraints can help in this regard.

Acknowledgements

This work was supported by the Innovation Fund Denmark project OPTI_MADE_BLADE, grant no. 75-2014-3. This support is gratefully acknowledged. The second author would like to thank Science Foundation Ireland (SFI) for funding Spatially and Temporally VARIable COMPosite Structures (VARICOMP) Grant No. (15/RP/2773) under its Research Professor programme.

References

D. B. Adams, L. T. Watson, Z. Gürdal, and C. M. Anderson-Cook. Genetic algorithm optimization and blending of composite laminates by locally reducing laminate thickness. *Advances in Engineering Software*, 35(1):35–43, jan 2004. ISSN 0965-9978. doi: 10.1016/J.ADVENGSOFT.2003.09.001.

A. Albanesi, F. Bre, V. Fachinotti, and C. Gebhardt. Simultaneous ply-order, ply-number and ply-drop optimization of laminate wind turbine blades using the inverse finite element method. *Composite Structures*, 184:894–903, jan 2018. ISSN 0263-8223. doi: 10.1016/J.COMPSTRUCT.2017.10.051.

R. H. Barnes and E. V. Morozov. Structural optimisation of composite wind turbine blade structures with variations of internal geometry configuration. *Composite Structures*, 152:158–167, 2016. ISSN 02638223. doi: 10.1016/j.compstruct.2016.05.013.

M. W. Bloomfield, J. E. Herencia, and P. M. Weaver. Enhanced two-level optimization of anisotropic laminated composite plates with strength and buckling constraints. *Thin-Walled Structures*, 47(11):1161–1167, nov 2009. ISSN 0263-8231. doi: 10.1016/J.TWS.2009.04.008.

C. L. Bottasso, F. Campagnolo, A. Croce, S. Dilli, F. Gualdoni, and M. B. Nielsen. Structural optimization of wind turbine rotor blades by multilevel sectional/multibody/3D-FEM analysis. *Multibody System Dynamics*, 32(1):87–116, 2014. ISSN 13845640. doi: 10.1007/s11044-013-9394-3.

M. Bruyneel. SFP—a new parameterization based on shape functions for optimal material selection: application to conventional composite plies. *Structural and Multidisciplinary Optimization*, 43(1):17–27, jan 2011. ISSN 1615-147X. doi: 10.1007/s00158-010-0548-0.

M. Bruyneel and P. Duysinx. Note on singular optima in laminate design problems. *Structural and Multidisciplinary Optimization*, 31(2):156–159, feb 2006. ISSN 1615-147X. doi: 10.1007/s00158-005-0569-2.

M. Bruyneel, P. Duysinx, C. Fleury, and T. Gao. Extensions of the Shape Functions with Penalization Parameterization for Composite-Ply Optimization. *AIAA Journal*, 49(10):2325–2329, oct 2011. ISSN 0001-1452. doi: 10.2514/1.J051225.

N. Buckney, S. Green, A. Pirrera, and P. M. Weaver. On the structural topology of wind turbine blades. *Wind Energy*, 16(4):545–560, may 2013. ISSN 10954244. doi: 10.1002/we.1504.

J. Chen, Q. Wang, W. Z. Shen, X. Pang, S. Li, and X. Guo. Structural optimization study of composite wind turbine blade. *Materials & Design*, 46:247–255, 2013. ISSN 0261-3069. doi: https://doi.org/10.1016/j.matdes.2012.10.036.

H.-T. Fan, H. Wang, and X.-H. Chen. An optimization method for composite structures with ply-drops. *Composite Structures*, 136:650–661, feb 2016. ISSN 0263-8223. doi: 10.1016/J.COMPSTRUCT.2015.11.003.

L.-C. Forcier and S. Joncas. Development of a structural optimization strategy for the design of next generation large thermoplastic wind turbine blades. *Structural and Multidisciplinary Optimization*, 45(6):889–906, jun 2012. ISSN 1615-147X. doi: 10.1007/s00158-011-0722-z.

T. Gao, W. Zhang, and P. Duysinx. A bi-value coding parameterization scheme for the discrete optimal orientation design of the composite laminate. *International Journal for Numerical Methods in Engineering*, 91(1):98–114, jul 2012. ISSN 00295981. doi: 10.1002/nme.4270.

T. Gao, W. H. Zhang, and P. Duysinx. Simultaneous design of structural layout and discrete fiber orientation using bi-value coding parameterization and volume constraint. *Structural and Multidisciplinary Optimization*, 48(6):1075–1088, dec 2013. ISSN 1615-147X. doi: 10.1007/s00158-013-0948-z.

P. E. Gill, W. Murray, and M. A. Saunders. SNOPT: An SQP Algorithm for Large-Scale Constrained Optimization. *SIAM Review*, 47(1):99–131, jan 2005. ISSN 0036-1445. doi: 10.1137/S0036144504446096.

C. F. Hvejsel and E. Lund. Material interpolation schemes for unified topology and multi-material optimization. *Structural and Multidisciplinary Optimization*, 43(6):811–825, jun 2011. ISSN 1615-147X. doi: 10.1007/s00158-011-0625-z.

S. T. IJsselmuiden, M. M. Abdalla, O. Seresta, and Z. Gürdal. Multi-step blended stacking sequence design of panel assemblies with buckling constraints. *Composites Part B: Engineering*, 40(4):329–336, jun 2009. ISSN 1359-8368. doi: 10.1016/J.COMPOSITESB.2008.12.002.

F.-X. Irisarri, A. Lasseigne, F.-H. Leroy, and R. Le Riche. Optimal design of laminated composite structures with ply drops using stacking sequence tables. *Composite*

Structures, 107:559–569, jan 2014. ISSN 0263-8223. doi: 10.1016/J.COMPSTRUCT.2013.08.030.

F.-X Irisarri, D. Peeters, and M. Abdalla. Optimisation of ply drop order in variable stiffness laminates. *Composite Structures*, 152:791–799, sep 2016. ISSN 0263-8223. doi: 10.1016/J.COMPSTRUCT.2016.05.076.

J.-S. Kim, C.-G. Kim, and C.-S. Hong. Optimum design of composite structures with ply drop using genetic algorithm and expert system shell. *Composite Structures*, 46 (2):171–187, oct 1999. ISSN 0263-8223. doi: 10.1016/S0263-8223(99)00052-5.

B. P. Kristinsdottir, Z. B. Zabinsky, M. E. Tuttle, and S. Neogi. Optimal design of large composite panels with varying loads. *Composite Structures*, 51(1):93–102, jan 2001. ISSN 0263-8223. doi: 10.1016/S0263-8223(00)00128-8.

D. Liu, V. V. Toroporov, O. M. Querin, and D. C. Barton. Bilevel Optimization of Blended Composite Wing Panels. *Journal of Aircraft*, 48(1):107–118, jan 2011. ISSN 0021-8669. doi: 10.2514/1.C000261.

E. Lund. Buckling topology optimization of laminated multi-material composite shell structures. *Composite Structures*, 91(2):158–167, 2009. ISSN 02638223. doi: 10.1016/j.compstruct.2009.04.046.

E. Lund. Discrete Material and Thickness Optimization of laminated composite structures including failure criteria. *Structural and Multidisciplinary Optimization*, 57(6): 2357–2375, dec 2018. ISSN 1615-147X. doi: 10.1007/s00158-017-1866-2.

E. Lund, L. Johansen, C. F. Hvejsel, and E. Olesen. Multi-Criteria Multi-Material Topology Optimization of Laminated Composite Structures. In *12th AIAA/ISSMO Multidisciplinary Analysis and Optimization Conference*, Reston, Virigina, sep 2008. American Institute of Aeronautics and Astronautics. ISBN 978-1-60086-982-2. doi: 10.2514/6.2008-5897.

MUST. The MUltidisciplinary Synthesis Tool (MUST), Department of Materials and Production, Aalborg University, 2018.

S. Nikbakt, S. Kamarian, and M. Shakeri. A review on optimization of composite structures Part I: Laminated composites. *Composite Structures*, 195:158–185, jul 2018. ISSN 0263-8223. doi: 10.1016/J.COMPSTRUCT.2018.03.063.

S. Panda and R. Natarajan. Analysis of laminated composite shell structures by finite element method. *Computers & Structures*, 14(3-4):225–230, jan 1981. ISSN 0045-7949. doi: 10.1016/0045-7949(81)90008-0.

D. Peeters and M. M. Abdalla. Optimization of Ply Drop Locations in Variable-Stiffness Composites. *AIAA Journal*, 54(5):1760–1768, may 2016. ISSN 0001-1452. doi: 10.2514/1.J054369.

A. Pirrera, M. Capuzzi, N. Buckney, and P. Weaver. Optimization of Wind Turbine Blade Spars. In *53rd AIAA/ASME/ASCE/AHS/ASC Structures, Structural Dynamics*

and Materials Conference 20th AIAA/ASME/AHS Adaptive Structures Conference 14th AIAA, Reston, Virigina, apr 2012. American Institute of Aeronautics and Astronautics. ISBN 978-1-60086-937-2. doi: 10.2514/6.2012-1500.

O. Sigmund. Morphology-based black and white filters for topology optimization. *Structural and Multidisciplinary Optimization*, 33(4-5):401–424, feb 2007. ISSN 1615-147X. doi: 10.1007/s00158-006-0087-x.

J. H. Sjølund and E. Lund. Structural gradient based sizing optimization of wind turbine blades with fixed outer geometry. *Composite Structures*, 203:725–739, nov 2018. ISSN 02638223. doi: 10.1016/j.compstruct.2018.07.031.

J. H. Sjølund, D. Peeters, and E. Lund. A new thickness parameterization for Discrete Material and Thickness Optimization. *Structural and Multidisciplinary Optimization*, 58(5):1885–1897, nov 2018. ISSN 1615-147X. doi: 10.1007/s00158-018-2093-1.

G. Soremekun, Z. Gürdal, C. Kassapoglou, and D. Toni. Stacking sequence blending of multiple composite laminates using genetic algorithms. *Composite Structures*, 56 (1):53–62, apr 2002. ISSN 0263-8223. doi: 10.1016/S0263-8223(01)00185-4.

R. Sørensen and E. Lund. Thickness filters for gradient based multi-material and thickness optimization of laminated composite structures. *Structural and Multidisciplinary Optimization*, 52(2):227–250, 2015. ISSN 16151488. doi: 10.1007/s00158-015-1230-3.

S. N. Sørensen and E. Lund. Topology and thickness optimization of laminated composites including manufacturing constraints. *Structural and Multidisciplinary Optimization*, 48(2):249–265, aug 2013. ISSN 1615-147X. doi: 10.1007/s00158-013-0904-y.

S. N. Sørensen, R. Sørensen, and E. Lund. DMTO – a method for Discrete Material and Thickness Optimization of laminated composite structures. *Structural and Multidisciplinary Optimization*, 50(1):25–47, jul 2014. ISSN 1615-147X. doi: 10.1007/s00158-014-1047-5.

J. Stegmann and E. Lund. Discrete material optimization of general composite shell structures. *International Journal for Numerical Methods in Engineering*, 62(14):2009–2027, 2005. ISSN 00295981. doi: 10.1002/nme.1259.

M. Stolpe and K. Svanberg. An alternative interpolation scheme for minimum compliance topology optimization. *Structural and Multidisciplinary Optimization*, 22(2): 116–124, sep 2001. ISSN 1615-147X. doi: 10.1007/s001580100129.

O. T. Thomsen. Sandwich materials for wind turbine blades - Present and future. *Journal of Sandwich Structures and Materials*, 11(1):7–26, jan 2009. ISSN 10996362. doi: 10.1177/1099636208099710.

Y. Xu, J. Zhu, Z. Wu, Y. Cao, Y. Zhao, and W. Zhang. A review on the design of laminated composite structures: constant and variable stiffness design and topology optimization. *Advanced Composites and Hybrid Materials*, pages 1–18, apr 2018. ISSN 2522-0128. doi: 10.1007/s42114-018-0032-7.